Research Article | **Open Access**

Microstructures

Wang *et al*. *Microstructures* **2026**, *5*, 2026036 **DOI:**10.20517/microstructures.2025.04

Additively manufactured Ti-6Al-4V/Ta bimetal: from neutron diffraction residual stress analysis to wear and bioproperty testings

Hao Wang[1], Ke Ma[1,2], Jincheng Tang[2,3], Jing Zhao[2], Hancong Chen[2], Yinghao Zhou[4], Xiaoping Luo[5], Jiazheng Hao[6,7], Lunhua He[6,8,9], Ming Yan[2,3]

Keywords:
Powder bed fusion-laser beam, neutron diffraction, residual stress, bimetal

Citation: Wang, H.; Ma, K.; Tang, J.; Zhao, J.; Chen, H.; Zhou, Y.; Luo, X.; Hao, J.; He, L.; Yan, M. Additively manufactured Ti-6Al-4V/Ta bimetal: from neutron diffraction residual stress analysis to wear and bioproperty testings. *Microstructures* **2026**, *5*, 2026036. https://dx.doi.org/10.20517/microstructures.2025.04

Received: 11 Jan 2025
First Decision: 14 Apr 2025
Revised: 17 May 2025
Accepted: 3 Jun 2025
Published: 30 Mar 2026

Academic Editor: Yandong Wang
Copy Editor: Shu-Yuan Duan
Production Editor: Shu-Yuan Duan

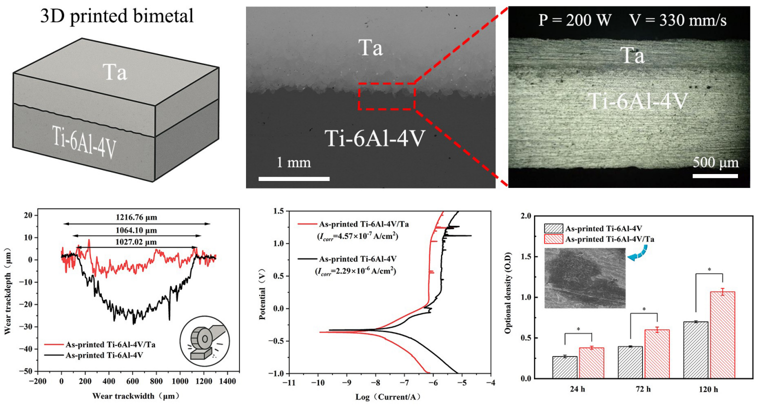

The bimetal exhibited much improved wear resistance, corrosion resistance, and good biocompatibility

Abstract

Powder bed fusion-laser beam prepared Ti-6Al-4V/Ta bimetals can be well-suited for advanced biomedical applications. However, a few issues remain unsolved, including (a) understanding of residual stress distribution and its level in as-printed bimetal; and (b) wear and bio properties of the bimetal. This study aims to address these points through a series of investigations, including residual stress analysis by neutron diffraction, printing optimization, and analysis of heat treatment effect on the properties. It was discovered that the residual stress is highly related to the temperature gradient and Young's modulus. In the interface region of the as-printed bimetal, the residual stress was reduced and inverted compared to the as-printed Ta alone, changing from ~ (140-180) MPa (tensile) to ~ (30-70) MPa (compressive), which may have helped the Ta layer bond effectively with the Ti-6Al-4V matrix. Meanwhile, a high residual stress (~ 390 MPa) in the Ti-6Al-4V part of

---

[1]State Key Laboratory of Radio Frequency Heterogeneous Integration, College of Mechatronics and Control Engineering, Shenzhen University, Shenzhen 518060, Guangdong, China.
[2]Department of Materials Science and Engineering, Southern University of Science and Technology, Shenzhen 518055, Guangdong, China.
[3]Jiaxing Research Institute, Southern University of Science and Technology, Shenzhen 518055, Guangdong, China.
[4]Department of Mechanical Engineering, City University of Hong Kong, Hong Kong 999077, Hong Kong.
[5]Nanjing Stomatological Hospital Medical School of Nanjing University, Nanjing 210008, Jiangsu, China.
[6]Spallation Neutron Source Science Center, Dongguan, 523803, Guangdong, China.
[7]Institute of High Energy Physics, Chinese Academy of Sciences, Beijing 100049, China.
[8]Beijing National Laboratory for Condensed Matter Physics, Institute of Physics, Chinese Academy of Sciences, Beijing 100190, China.
[9]Songshan Lake Materials Laboratory, Dongguan 523808, Guangdong, China.

Correspondence to: Prof. Ming Yan, Department of Materials Science and Engineering, Southern University of Science and Technology, Shenzhen 518055, Guangdong, China. E-mail: yanm@susech.edu.cn; Dr. Yinghao Zhou, Department of Mechanical Engineering, City

University of Hong Kong, Hong Kong 999077, Hong Kong. E-mail: yzhou572@cityu.edu.hk

the as-printed bimetal justifies the need for heat treatment. After heat treatment, the bimetal exhibited good biocompatibility and much improved wear and corrosion resistance compared to Ti-6Al-4V alone. These improvements may be attributed to the formation of tantalum oxide during friction and corrosion processes. Ta layer can also improve the biocompatibility due to its intrinsic noncytotoxic feature.

INTRODUCTION

Compared with other orthopedic materials such as CoCrMo and stainless steels, Ti-6Al-4V has advantages such as low density, high specific strength, good biocompatibility, and a Young's modulus closer to that of the human bone structure[1,2]. It has been widely used in dental implants, bone nails, hip joints, and cardiovascular stents[1,2]. However, Ti-6A1-4V also has notable shortcomings. First, its alloying elements, *i.e.*, V and A1, may affect the synthesis and metabolism of phosphate and/or lead to symptoms such as neurological disorders and Alzheimer's disease[3,4]. Second, its wear resistance is far from ideal[5]. In fact, its low shear resistance and work-hardening tendency exacerbate adhesive or abrasive wear, among others, often resulting in unsatisfactory friction and wear behaviors. In clinical trials, even when Ti-6A1-4V is partnered with soft materials such as polyethylene, debris generated due to the wear process can cause aseptic loosening of the Ti implants[6,7].

Ta has excellent biomechanical properties, corrosion resistance, and biocompatibility, and it has been increasingly used in clinical implants such as hip joints, patella joints, and vertebrae[8-10]. It has also been suggested that Ta implantation promotes the formation of hydroxyapatite *in vivo*, thereby inducing cell attachment and proliferation[11]. Matsuno *et al.*[12] implanted Ta into the femur of white mice and studied its physiological responses. They found no inflammation in the surrounding tissues, and the Ta implant remained undegraded after 4 weeks, indicating good corrosion resistance. Furthermore, Ta demonstrates considerable wear resistance; its higher Young's modulus compared to Ti and Ti alloys reduces the probability of wear erosion[13]. However, major drawbacks of Ta include its high material cost and high density (~ 16.6 g/cm^3), which far exceeds that of human bone (~ 1.7 g/cm^3)[8-10] or Ti-based materials (~ 4.5 g/cm^3)[1,2] [Table 1].

A combination of Ti and Ta, therefore, shows promise by leveraging the advantages of both materials, *i.e.*, the high strength of the Ti-6Al-4V alloy and the excellent surface properties of Ta, such as superior wear resistance and biocompatibility. Laser-based additive manufacturing (AM) such as powder bed fusion-laser beam (PBF-LB) is well-suited to producing such multi-material structures. These AM methods can also make customized products and provide metallurgical bonding between metals, thus ensuring good mechanical properties[14,15].

Progress and problems regarding PBF-LB-prepared Ta and/or Ti-6Al-4V bimetals include:

(1) Bulk and/or porous Ta has been printed using PBF-LB and other AM approaches, and the printing parameters and their effects on microstructure and mechanical properties have been detailed in a few typical studies[16-21]. High-performance, as-printed Ta has been realized.

(2) Multi-material printing involving Ti or Ti-6Al-4V and Ta mainly focused on the fabrication of graded Ti/Ta parts or Ti alloys doped with different Ta contents, rather than the surface modification of Ti with Ta. Meanwhile, most of these works mainly studied the printability of the TiTa alloys[22-25]. A few important issues such as residual stress distribution characteristics, mechanical behavior, and wear and corrosion

Table 1. Fundamental properties of Ta and Ti-6Al-4V[3,27,28]

Material	Melting point	Density	Thermal conductivity	Linear expansion coefficient	Young's modulus	Tensile strength	Hardness	Ref.
Ta	3269 K	16.6 g/cm^3	54.4 W·m^{-1}·K^{-1}	6.5×10^{-6}·K^{-1}	186 GPa	205 MPa	110 HV	[27,28]
Ti-6Al-4V	1940 K	4.5 g/cm^3	13.8 W·m^{-1}·K^{-1}	8.2×10^{-6}·K^{-1}	110 GPa	960 MPa	350 HV	[3]

resistances remain insufficiently studied, especially in the bimetals[26].

(3) Ta and Ti-6Al-4V exhibit many differences in their material properties [Table 1][27,28]. For instance, their melting points differ by more than 1,000 °C, which can be problematic as the high energy input that is necessary to remelt Ta may cause evaporation of Ti-6Al-4V, leaving pores in the microstructure of the resulting bimetal.

Thus, the purpose of this work is to explore the possibility of creating advanced Ti-6Al-4V/Ta bimetals and to address existing issues, such as residual stress distribution, optimization of the printing process, and enhancement of material properties. A systematic and comprehensive study was conducted. Printing optimization was employed to achieve the best possible as-printed bimetal samples. Neutron diffraction was employed to study the residual stress in these samples, and heat treatment was performed to further optimize the bimetal structure. A series of investigations were subsequently performed to evaluate the microstructure, mechanical properties, wear properties, electrochemical corrosion properties, and *in vitro* cell compatibility. The results show that the prepared bimetals have enhanced properties compared with Ti-6Al-4V, particularly in terms of wear and corrosion resistance, demonstrating a feasible route to achieve high-performance orthopedic materials by utilizing the properties of the two distinct materials.

MATERIALS AND METHODS

Raw materials

The powder feedstocks used in this study were pre-alloyed, gas-atomized Ti-6Al-4V powder and gas-atomized Ta powder [Table 2]. The particle size distributions were tested using a Malvern LS-609 laser particle size analyzer, with Dv (50) values of 35.2 μm for the Ti-6Al-4V powder and 27.9 μm for the Ta powder. scanning electron microscope (SEM) images and particle size distribution results are shown in Figure 1A-D.

PBF-LB process and heat treatment

The metal printer used was an SLM Solution ® 125HL. The bimetallic printing process was conducted as follows: (a) Ti-6Al-4V was printed first using fixed parameters, *i.e.*, laser power of 275 W, scanning speed of 1,100 mm/s, hatch distance of 0.12 mm, and layer thickness of 0.03 mm; (b) Printing was then paused to replace the Ti-6Al-4V powder with Ta powder; (c) Approximately 1 mm of Ta was subsequently printed on top of the already printed Ti-6Al-4V. For Ta printing, the layer thickness (0.03 mm) and hatch distance (0.08 mm) were kept constant, while the other parameters were varied for optimization [Table 3]. The corresponding energy density was calculated using the following Equation 1[29]:

$$E = \frac{P}{v \times h \times s} \tag{1}$$

where P represents laser power, v for laser scanning speed, h for hatch distance, and s for layer thickness.

To release residual stress and study the effect of heat treatment on the as-printed samples, three different heat treatments were applied: 550 °C, 750 °C, and 950 °C, each for 2h. The samples were heated at a rate of 10

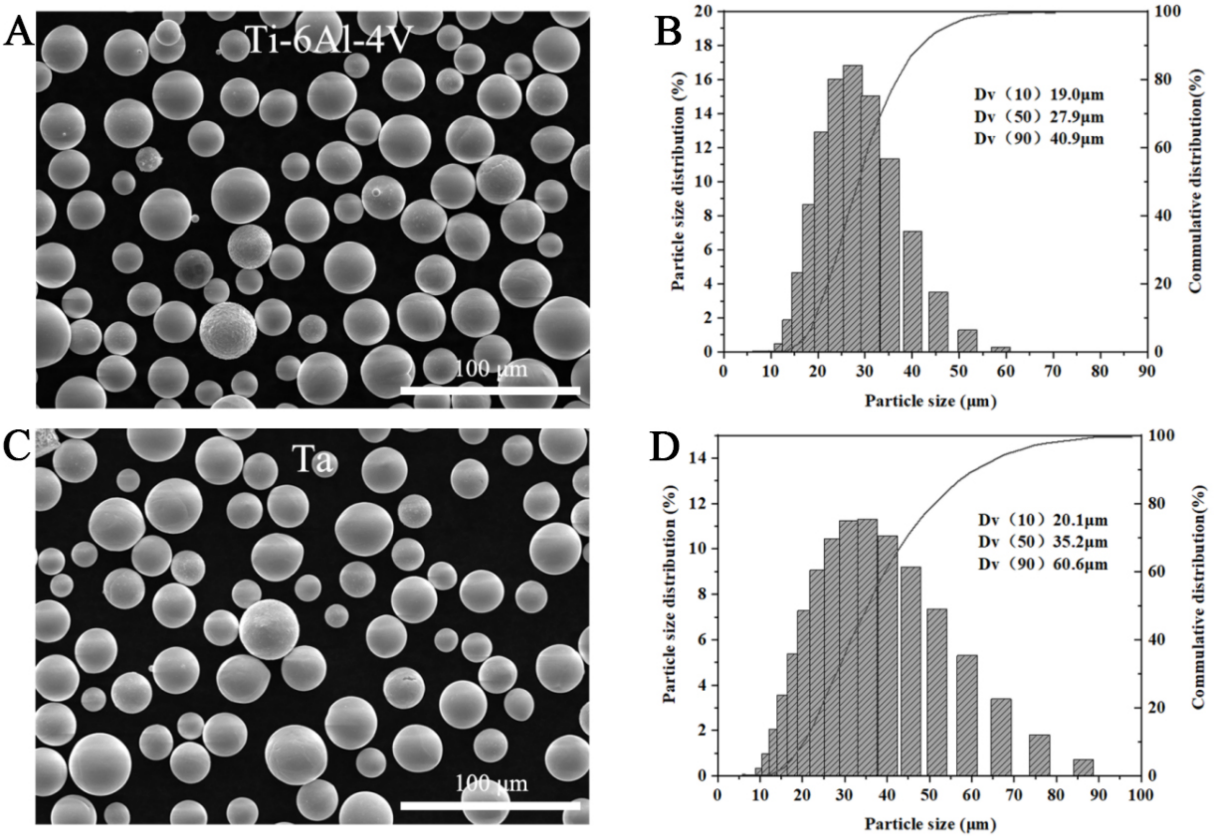

Figure 1. Powder morphology and particle size: (A) Morphological characteristics of Ti-6Al-4V powder; (B) Ti-6Al-4V particle size distribution map; (C) Morphological characteristics of Ta powder; and (D) Ta particle size distribution map.

Table 2. Chemical composition of the two powders used (wt.%)

Powder type	Ti	Ta	Al	V	Fe	C	N	O	H	Others
Ti-6Al-4V	Bal.	-	6.15	3.95	0.03	0.04	< 0.005	≤ 0.20	≤ 0.015	≤ 0.5
Ta	-	Bal.	-	-	0.005	0.01	0.005	0.015	0.0015	≤ 0.01

Table 3. Printing parameters for Ta

Sample	V (mm/s)	P (W)	Energy density (J/mm³)	Relative density (%)
#1	240	150	260.42	97.02
#2	250	150	250	94.55
#3	260	150	240.38	92.59
#4	270	150	231.48	94.68
#5	280	150	223.21	86.39
#6	290	150	215.52	83.67
#7	330	200	252.53	99.43
#8	340	200	245.10	95.01
#9	350	200	238.10	87.89
#10	360	200	231.48	89.02
#11	370	200	225.23	88.76
#12	380	200	219.30	85.68

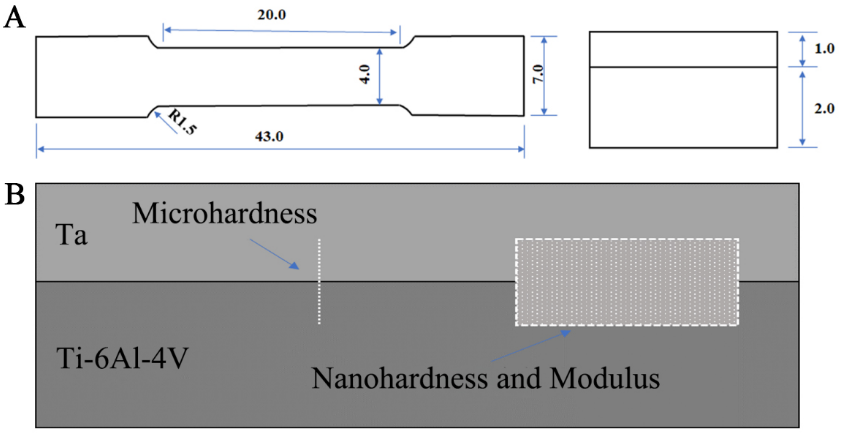

Figure 2. (A) Sample dimensions for the tensile test; and (B) setup for the nanohardness and modulus tests.

°C/min and subsequently cooled within the furnace. The rationale for choosing these temperatures is as follows: For pure Ta, its stress relief temperature is normally around 900 °C, while the recrystallization temperature is between 980 ~ 1,200 °C[30]. For the Ti-6Al-4V alloy, the β-transus temperature is ~ 980 °C, the $\alpha + \beta$ phase range is 600-980 °C, and the martensite phase transformation starts at ~ 610 °C[31].

Microstructural characterization and mechanical properties testing

The dimensions of the tensile samples are shown in Figure 2A. A schematic of the bimetal is shown in Figure 2B, where a Ta layer (~ 1 mm thick) is printed on the top of a Ti-6Al-4V substrate (~ 2 mm thick). Room temperature tensile tests were performed using a universal testing machine (Instron3382) at a strain rate of 0.2 mm/min. Three samples were tested for each group, and the results were averaged.

Microhardness was measured using an FM-ARS9000 Vickers microhardness tester. A total of 26 points were selected on each sample for testing, with a spacing of 0.1 mm between points [Figure 2B]. The test load was 0.98 N (equivalent to 100 gf), with a holding time of 15 s. The average value was calculated from three repeated measurements. Nanohardness testing was conducted using a TI950 nanoindenter (Hysitron, USA) with a load of 100 mN. The loading and unloading times were 5 s each, with a holding time of 2 s. Three experimental results were averaged. Young's modulus was also measured using the same equipment. The specific area used for the modulus test is indicated in Figure 2B.

Friction and wear tests were conducted at room temperature using a ball-on-disc dry friction and wear method. The friction pair consisted of a Φ5.556 mm Si_3N_4 ceramic ball rotating at a speed of 200 r/min. The applied load was 6 N, and friction time was 15 min. The average value was used after repeating the test three times. For the study of the friction marks, a laser confocal microscope (LEXT OLS4000, Olympus, Japan) was used. Each mark was measured at three different positions, and the average value was used.

An optical microscope (OM, model LEICADM 2700M) was used to image porosity, and the result was subsequently analyzed using Image J software. A SEM (Zeiss Merlin, Germany) was used for microstructural analysis. An energy dispersive spectrometer (EDS) was used for compositional analysis, using a voltage of 20 kV and a current of 3000 pA. For XRD (MiniFlex600) analysis, the target material was Cu target Kα, with a voltage of 40 kV, a current of 15 mA, a step size of 0.02, and a scanning speed of 9°/min.

To construct the binary phase diagram of Ti-Ta, the ThermoCalc platform was used with the TCTI3:TT Ti-Alloys v3.1 database.

Table 4. Composition of the SBF solution (mM/PH7.4/37 °C)

Ion type	Na^+	K^+	Mg^+	$Ca2^+$	Cl^+	HCO^{3-}	HPO_4^{2-}	SO_4^{2-}
	142	5	1.5	2.5	148.8	4.2	1	0.5

SBF: Simulated body fluid.

Neutron diffraction analysis of the residual stress

Neutron diffraction measurements were performed on the general purpose powder diffractometer, BL18 beamline, in the China spallation neutron source. For the residual stress analysis, the gauge volume is controlled by the four-blade slits, neutron Kirkpatrick-Baez mirror, and radial collimators, and the general gauge volume is φ2 × 2 mm^3. A decoupled poisoned hydrogen moderator generates neutron pulses with a frequency of 25 Hz. 90 ± 20.5° ^{6}LiF/ZnS scintillation detectors (4 mm × 4 mm) were used for data collection. It took about 2 h to measure the stress of each point. More details about the beamline can be found in published references[32,33]. Two types of samples were analyzed in the neutron diffraction analysis: One was the as-printed Ti-6Al-4V/Ta bimetal, with dimensions of 10 mm × 9.5 mm × 5 mm; the other was the pure printed Ta, with dimensions of 10 mm × 5 mm × 3.5 mm. The samples were directly cut from the building substrate without any other polish process.

Electrochemical corrosion test

Electrochemical corrosion tests were conducted using a CHI760E (Shanghai Chenhua) electrochemical workstation. The sample to be tested served as the working electrode, with platinum as the counter electrode and a saturated calomel electrode (SCE) as the reference. During the open circuit potential (OCP) test, the scanning rate was set to 1 mV/s, with a total scanning duration of 7,200 s. For polarization curve measurements, the potential was scanned from -0.5 V to 1.5 V (*vs.* OCP) at a scan rate of 1 mV/s. To avoid the influence of the Ti-6Al-4V matrix, the remaining surface of the bimetal sample was sealed with resin and tape, leaving only a 1 mm^2 area of the test surface exposed. The sample was placed in a constant-temperature water bath at 37 °C to simulate the temperature of simulated body fluid (SBF) temperature. The composition of the SBF is shown in Table 4.

Biocompatibility testing

*Φ*10 mm bimetal discs were polished with 2,000 # sand paper to remove the surface oxide layer, then subjected to ultrasonic cleaning for 10 min in anhydrous alcohol with purities of 75% and 100%, respectively. The samples were sterilized using high-temperature and high-pressure treatment. MG-63 cells (human osteosarcoma cells, ATCC) were seeded onto the samples at a density of 4 × 10^4 cells/sample for 2 h, and then fixed at 4°C for 2 h using 2.5% glutaraldehyde ($C_5H_8O_2$). The sample surfaces were washed with phosphate buffer solution and dehydrated in a graded ethanol series (10%, 30%, 50%, 70%, 80%, 90%, and 100%), with each step lasting 10 min. The samples were then dried using a freeze-drying machine, followed by platinum coating for observation of cell adhesion.

MG-63 cells were seeded onto the samples in a 24-well tissue culture polystyrene plate at a density of 4 × 10^4 cells/sample, with each well containing 500 μL of culture medium. Cell proliferation was assessed using a CCK-8 assay (Shanghai Yisheng Biotechnology Co., Ltd, China) after incubation for 24, 72, and 120 h. The absorbance (optical density) of each well was measured at 450 nm using a microplate reader and software of Microplate Manager® 6, Version 6.3 (iMark, BIO-RAD, China). All biomedical data were analyzed using one-way ANOVA and are expressed as the mean ± standard deviation from at least three independent experiments. Statistical significance was defined as $P < 0.05$. The data were analyzed using SPSS 17.0.

Table 5. Physical properties of Ta and Ti-6Al-4V[3,27,28]

Property	Ta	Ti-6Al-4V
Specific heat capacity (J/mol/K)	$Cp = 24.37+(3.27 \times 10^{-3}) \cdot T$	$483+0.22 \cdot T$ (0K-1,268K) $413+0.18 \cdot T$ (1,268K-1,873K) $-2{,}524+1.74 \cdot T$ (1,873K-1,923K) 831 (Above 1,923K)
Thermal conductivity (W/m/K)	$\Lambda = 56.00+(11.00 \times 10^{-3}) \cdot T$	$1.25 + 0.015 \cdot T$ (0K-1,268K) $3.15+0.012 \cdot T$ (1,268K-1,873K) $-289.66+0.168 \cdot T$ (1,873K-1,923K) $-12.75+0.024 \cdot T$ (Above 1,923K)
Density (kg/m^3)	$16{,}680\,(1 + (6.5 + 0.34 \times 10^{-6} \cdot T + 0.12 \times 10^{-6} \cdot T^2) \times (T-300) \times 10^{-6})^3$	1,873
Melting point (K)	3,270	1,923
Melting latent heat (kJ/kg)	202	286
Laser absorptivity	0.374 (powder state) / 0.208 (liquid state)	4,430 (0K-1,873K) $-8{,}137 + 6.70 \cdot T$ (1,873K-1,923K) 4,122 (Above 1,923K)
Value of parameter M1	3.38×10^{-7}	0.374 (powder state) / 0.208 (liquid state)
Surface emissivity	0.208	1.82×10^{-6}

Comsol molten pool simulation

COMSOL Multiphysic6.0 commercial software was used to simulate temperature field characteristics within molten pools [34,35]. Key parameters for the simulation, such as specific heat capacity (C_p), thermal conductivity (K), density (ρ), *etc*., were obtained from the literature[3,27,28] [Table 5]. Detailed model descriptions are summarized in the Supplementary Materials.

Overall research flowchart

Figure 3 summarizes all the important steps involved in this study.

RESULTS AND DISCUSSION

Printing parameter optimization for the Ti-6Al-4V/Ta bimetal

Figure 4A and B shows the printing results obtained for the bimetal samples manufactured using laser power of 150 W and 200 W, respectively, with varying scanning speeds. It should be noted that the parameter optimizations mentioned here apply specifically to the top Ta layer, while the printing parameters for the bottom Ti-6Al-4V layer remained unchanged throughout the process. Figure 4 and Table 3 suggest that when the energy input is insufficient for the bimetal, such as ~ 220 J/mm^3, a large number of pores (> 10%) exist in the microstructure. Decreasing the scanning speed and increasing the energy density reduced the porosity to a low level of ~ 2%. The best results were obtained when the laser power was 200 W and the printing speed was 330 mm/s, achieving a relative density of ~ 99.5% and porosity of ~ 0.5%. A further higher energy density (*e.g.*, > 260 J/mm^3) should lead to a lowered density, as it is known that the Ti-6Al-4V alone has the best energy density of ~ 70 J/mm^3[1] and too high energy input tends to cause evaporation in the Ti-6Al-4V part.

The relative density results were verified using cross-sectional OM images, shown in Figure 5. The figure reveals that the samples produced using a laser power of 200 W and scanning speed of 330 mm/s had the lowest number of defects, consistent with the density measured in Figure 4.

The as-printed bimetal was further characterized using OM and low-magnification SEM, with the resultant images shown in Figure 6A and B, respectively. The results indicate a good surface finish and a pore-free bonding interface between the Ti-6Al-4V matrix and the Ta layer.

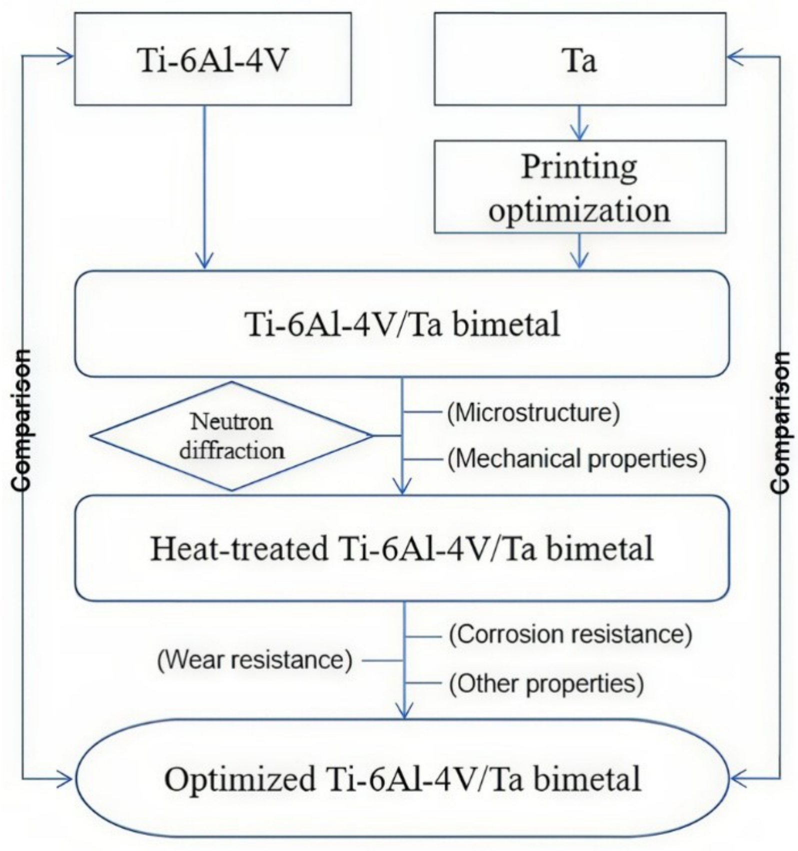

Figure 3. Overall research flow chart of the study.

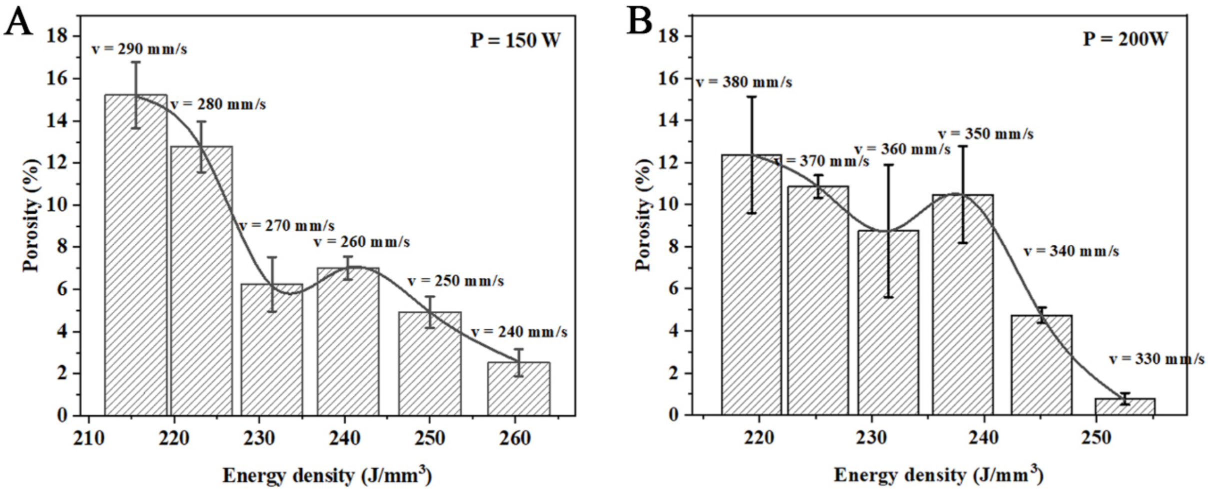

Figure 4. (A) Porosity and energy density of the bimetal when printed using 150 W laser power; and (B) porosity and energy density of the bimetal when printed using 200 W laser. The error bars represent the standard deviation.

To understand the bimetal printing process, a molten pool simulation was performed using the optimized printing parameters described above. The results are presented in Figure 7, where Figure 7A and C shows the data for Ti-6Al-4V and Figure 7B and D displays the results for Ta. The highest temperature achieved by the laser beam was ~ 3,500 K, exceeding the melting points of both Ti (1,940 K) and Ta (3,269 K), thereby ensuring metallurgical bonding. Since Ti-6Al-4V was printed first, followed by Ta, heat conduction from the

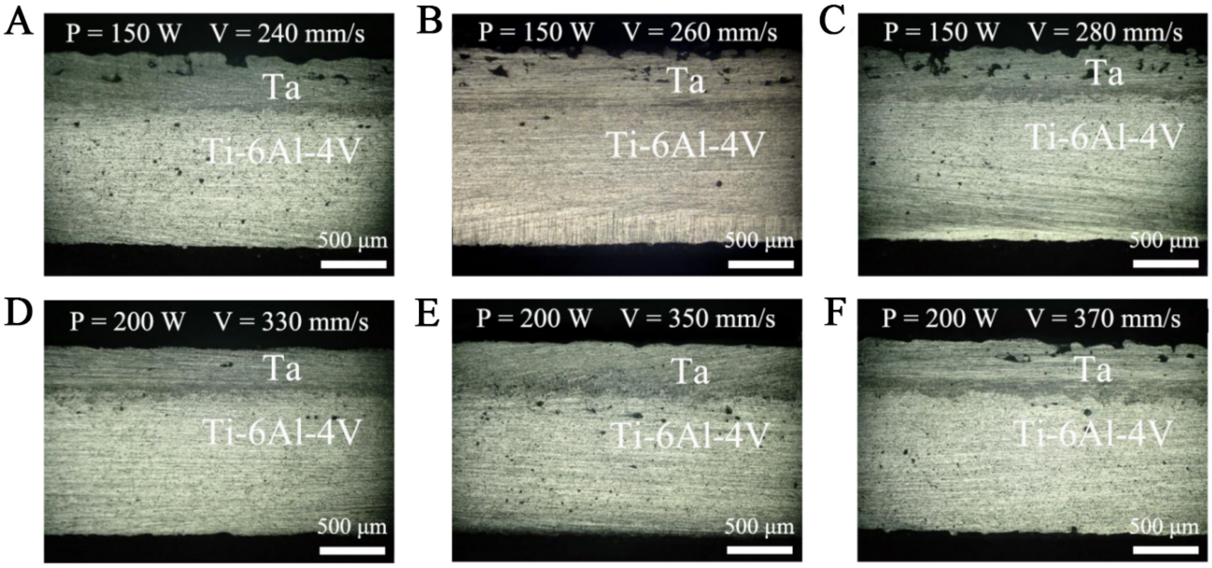

Figure 5. OM images for the bimetal printed using different parameters: (A) 150 W and 240 mm/s; (B) 150 W and 260 mm/s; (C) 150 W and 280 mm/s; (D) 200 W and 330 mm/s; (E) 200 W and 350 mm/s; and (F) 200 W and 370 mm/s. OM: Optical microscope.

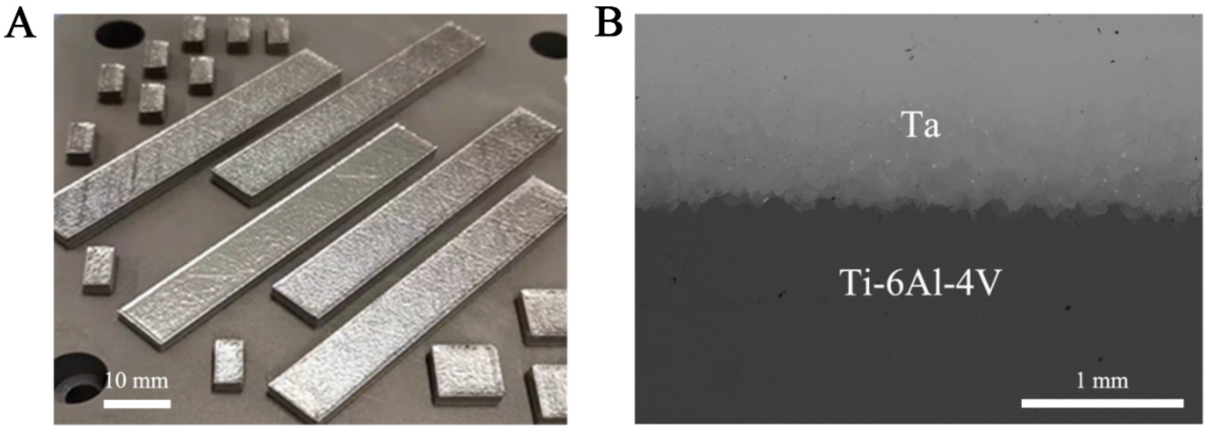

Figure 6. (A) Appearance of the as-printed bimetal; and (B) SEM image showing the interface between the Ti-6Al-4V layer and the Ta layer. SEM: Scanning electron microscope.

subsequently printed Ta layer was reduced, leading to a slightly prolonged molten pool duration at high temperatures.

Microstructure and mechanical properties of as-printed Ti-6Al-4V/Ta bimetal

Microstructural analysis

The microstructure of the printed bimetal was investigated using SEM with energy dispersive X-ray (SEM-EDX) spectroscopy, with a particular focus on the interface. The results are shown in Figure 8. The diffusion zone between the two distinctive metals was about 800 μm, as shown in Figure 8A and B. In this zone, all the constituent elements, namely Ti, Al, and V from the printed Ti-6Al-4V and Ta from the printed Ta, can be detected, indicating significant mutual diffusion between the two metals. However, Figure 8C also reveals the presence of a small amount of residual Ta powder, which is likely attributable to the high melting point of Ta (3,269 K).

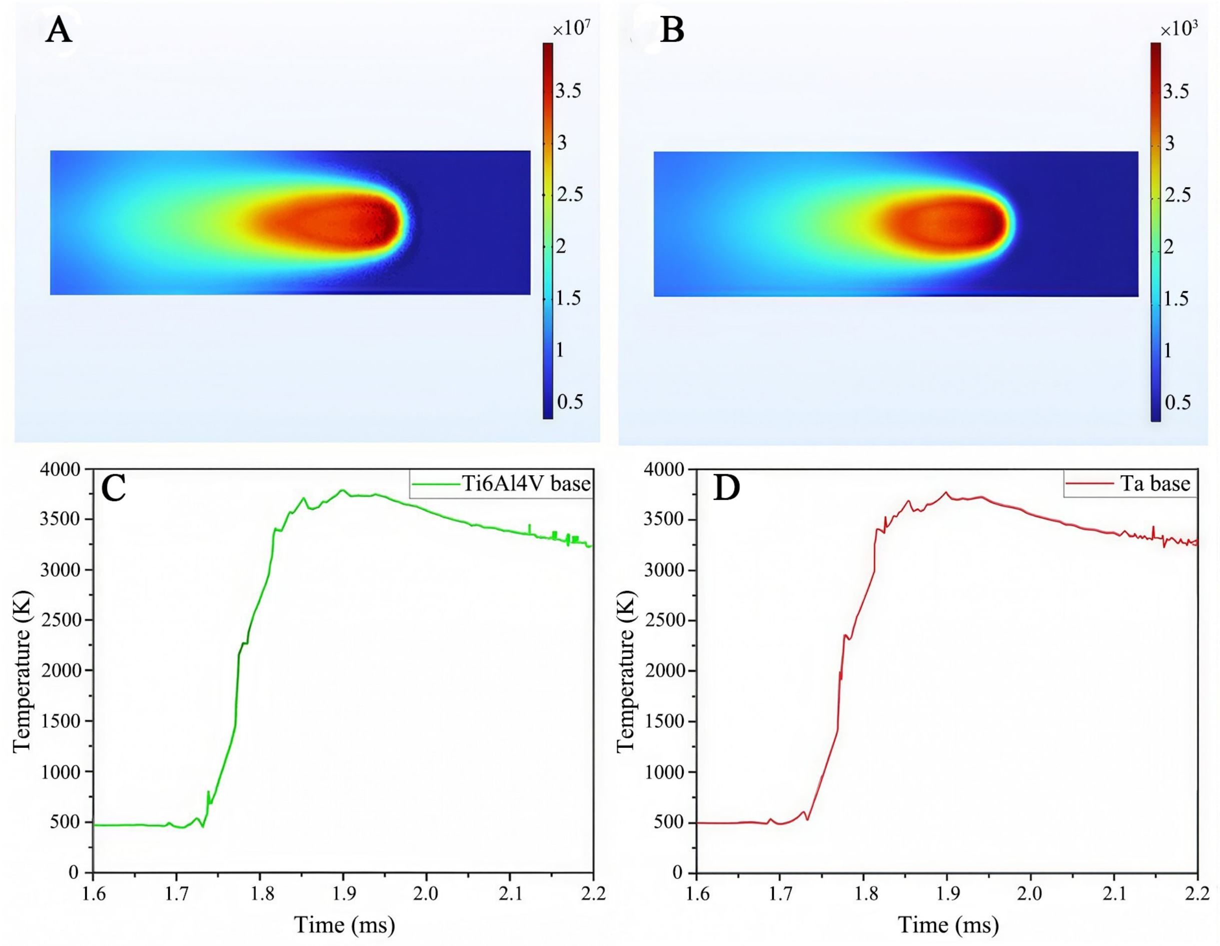

Figure 7. Molten pool simulation results for (A) and (C) Ti-6Al-4V; and (B) and (D) Ta.

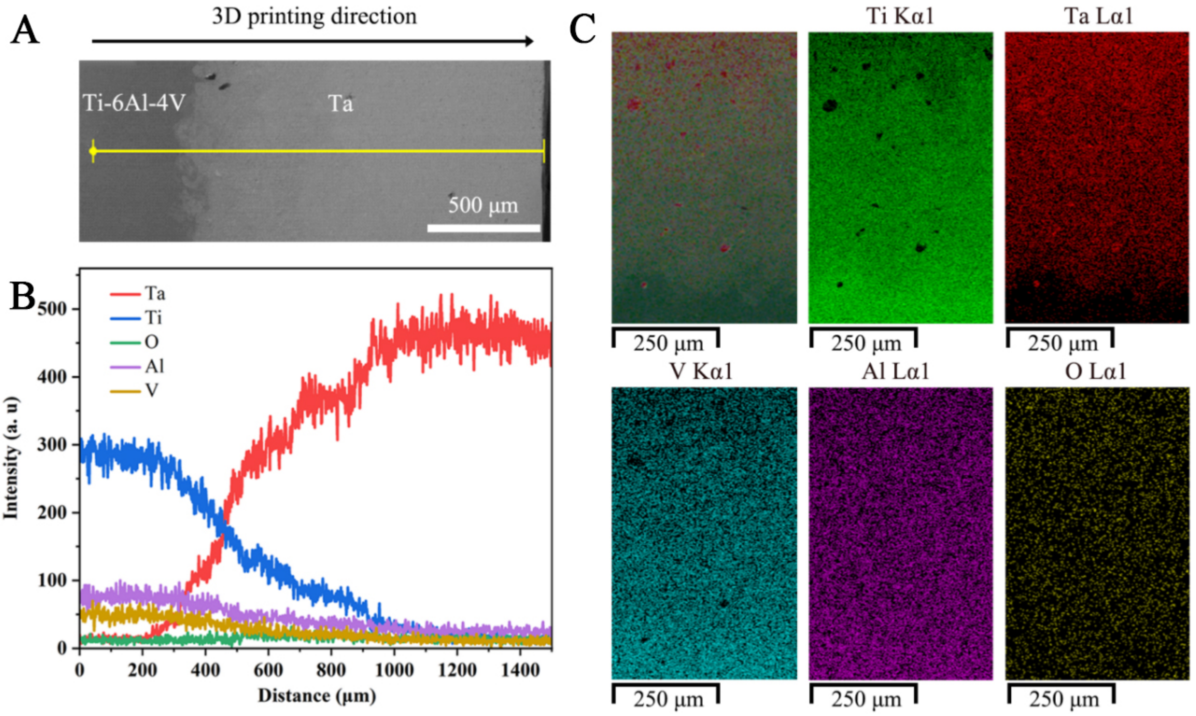

Figure 8. EDS spectra of the bimetallic interface binding zone: (A) scanned area; (B) line scan energy spectrum; and (C) surface scan energy spectrum. EDS: Energy dispersive spectrometer.

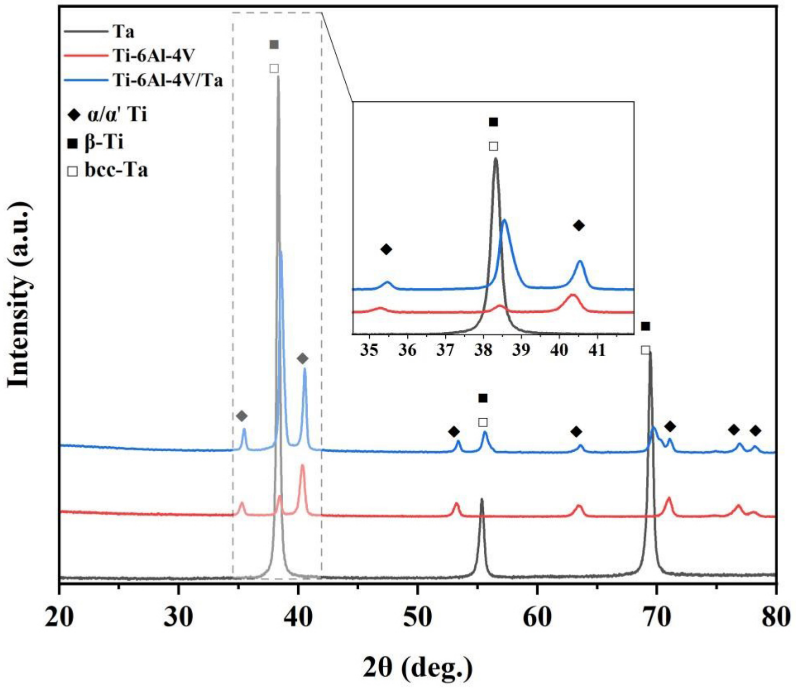

Figure 9. XRD spectra of the Ti-6Al-4V, Ta, and Ti-6Al-4V/Ta. XRD: X-ray diffractometer.

The SEM results were verified through XRD analysis [Figure 9]. It is evident that α'/α-Ti is the main phase for the printed Ti-6Al-4V, although some β phases (β-Ti) are also visible. Within the pure Ta side, a single bcc-structured phase (bcc-Ta) was observed, while all three phases were observed at the bimetal interface. The enlarged inset in Figure 9 further indicates that, compared to the pure Ta phase, the Ta detected in the interface area was slightly shifted toward a higher angle, indicating a reduced unit cell parameter possibly resulting from the partial replacement of Ta by other elements, particularly Ti. Another possible reason for the shifted peak is due to residual stress in the alloy.

Mechanical properties

Figure 10A shows the distribution of Vickers hardness across the entire sample. This Vickers hardness of the printed Ta was 247-254 HV0.1, while that of the matrix Ti-6Al-4V was 337-340 HV0.1, which are similar to previously reported results[27-28,36]. The Vickers hardness of the bonding zone was within the range of 279-290 HV0.1, likely due to the inter-diffusion between Ti-6Al-4V and Ta. Figure 10B shows the tensile stress–strain curve obtained for the Ti-6Al-4V/Ta bimetallic sample, demonstrating a tensile strength of ~934 MPa and a fracture elongation of 4.17%. The theoretical tensile strength R_{mj} of the bimetal can be calculated using Equation 2[37]:

$$R_{mj} = \frac{R_{m1} \times t_1 + R_{m2} \times t_2}{t_1 + t_2} \tag{2}$$

where R_{m1} and R_{m2} are the lower-limit standard values of the tensile strength of the substrate and added layer, respectively, and T_1 and T_2 are the thicknesses of the substrate and added layer, respectively. Based on the known thickness of each metal and the international standard for single Ti-6Al-4V and single Ta, the theoretical tensile strength of the Ti-6Al-4V/Ta bimetallic structure was calculated to be approximately 686 MPa[38,39]. The difference between the experimental and theoretical values may be caused by the fine microstructure and residual stress induced by the high cooling rate of the PBF-LB process. Thus, the higher strength of the as-printed Ti-6Al-4V/Ta bimetal (934 MPa) obtained here demonstrates the advantages of

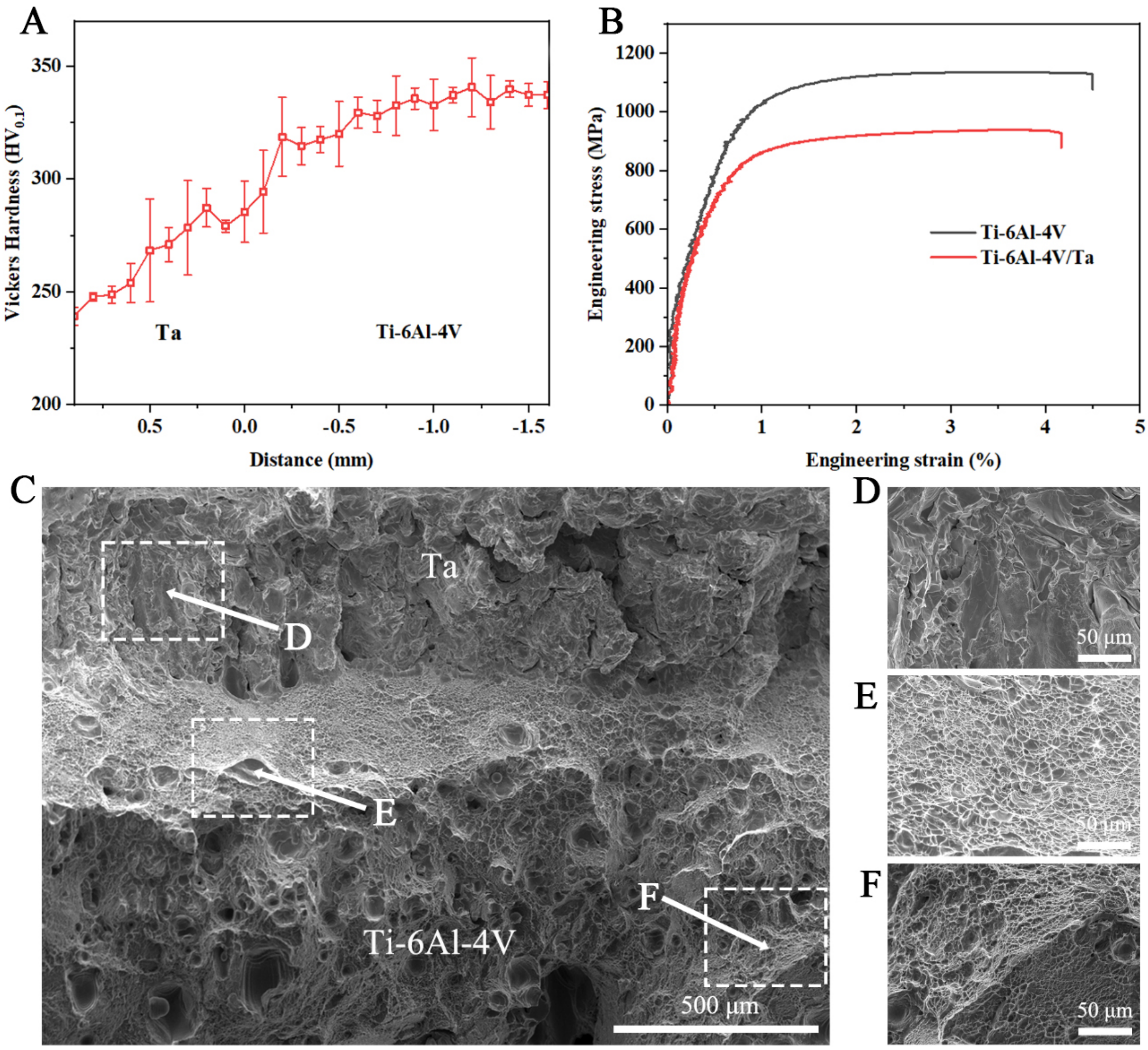

Figure 10. Mechanical properties of the as-printed bimetal using the best printing parameters: (A) Hardness* (The error bars represent the standard deviation); and (B) Tensile property; (C) Overall fracture morphology of the as-printed bimetal; (D-F) Enlarged images showing the fracture morphology at Ta layer, interfacial bonding region, and Ti6Al4V matrix, respectively. *Error limit and average value are shown for Figure 10A, where error limit is expressed as line segemant and average value is shown as square spot.

PBF-LB in the development of high-strength biomedical materials. The fracture surface was also characterized by SEM to determine the fracture mechanism. As shown in Figure 10C, the overall fracture surface shows distinct morphologies from the Ta layer to the Ti-6Al-4V matrix. The Ta layer shows a dissociation fracture model [Figure 10D], while the interfacial and Ti-6Al-4V matrix present ductile dimples [Figure 10E and F]. The compressive stress within the Ta/Ti6Al4V interface region may contribute to the bonding strength and thus improve the ductility.

Residual stress by neutron diffraction of as-printed Ti-6Al-4V/Ta bimetal

Neutron diffraction was used to evaluate the residual stress of the as-printed bimetal[32]. The pure Ta was analyzed first, followed by the as-printed bimetal.

Figure 11 shows the results for the Ta part, with Figure 11A showing the analysis points (Point 1 and Point 2) inside the as-printed Ta. In the middle of the sample, tensile residual stresses of 140-180 MPa were present in

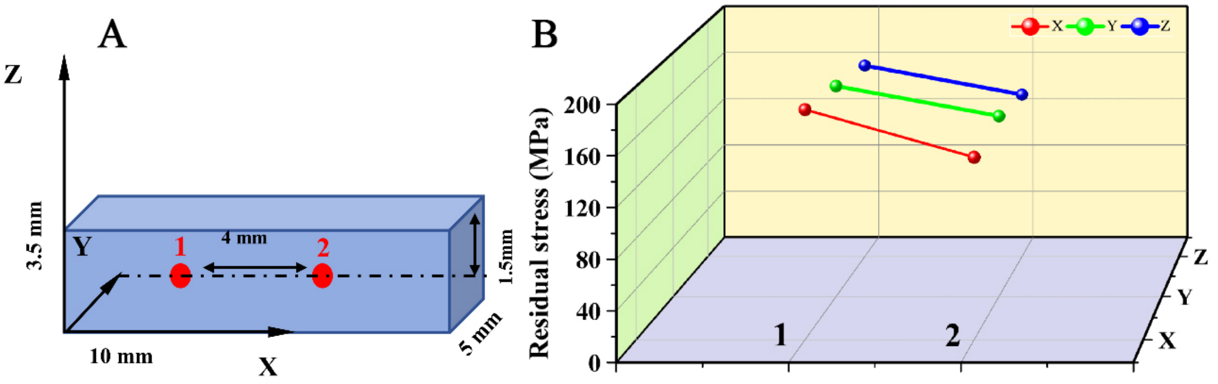

Figure 11. (A) Sample dimensions for the neutron diffraction analysis, with measurement locations indicated; and (B) Residual stress distributions in the X, Y, and Z directions.

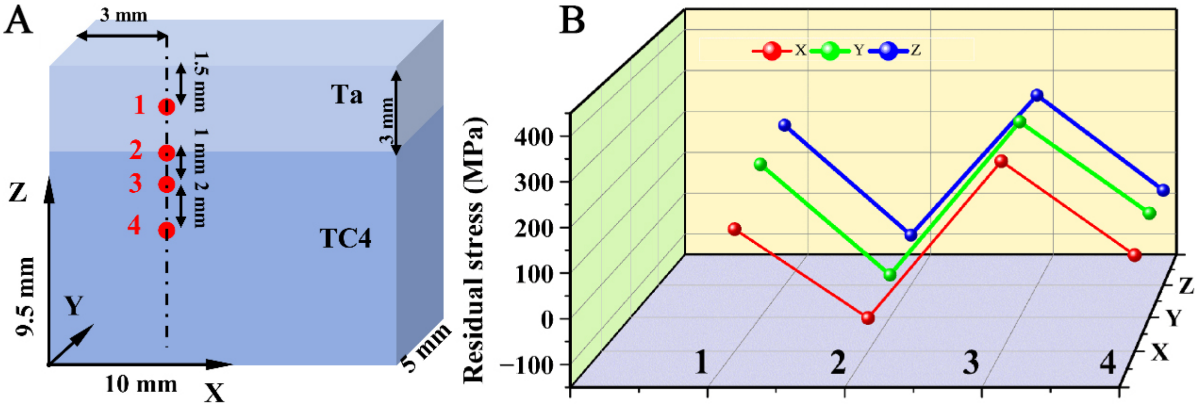

Figure 12. (A) Sample dimensions for the neutron diffraction analysis, with measurement locations indicated, and the corresponding results table; and (B) Residual stresses in the X, Y and Z directions.

Table 6. Residual stress for Ta alone and the as-printed Ti-6Al-4V/Ta bimetal

	Point	X	Y	Z
Ta	1	181.71 MPa	172.62 MPa	162.23 MPa
	2	144.05 MPa	147.95 MPa	137.56 MPa
Ti-6Al-4V/Ta	1	125.22 MPa	204.43 MPa	230.40 MPa
	2	-75.07 MPa	-51.70 MPa	-30.92 MPa
	3	359.30 MPa	391.10 MPa	390.04 MPa
	4	86.10 MPa	117.89 MPa	97.76 MPa

the *X*-, *Y*-, and *Z*- directions. Figure 11B shows the original experimental data, based on which residual stress has been determined in each direction[33,34] [Table 6].

A more comprehensive neutron diffraction analysis was conducted on the as-printed bimetal. Figure 12 shows the results for the analysis points inside the Ta alone (Point 1), in the interface bonding area (Point 2), and inside the Ti-6Al-4V (Point 3, which is closer to the interface, and Point 4, which is away from the interface) [Table 6]. The results show a few notable findings:

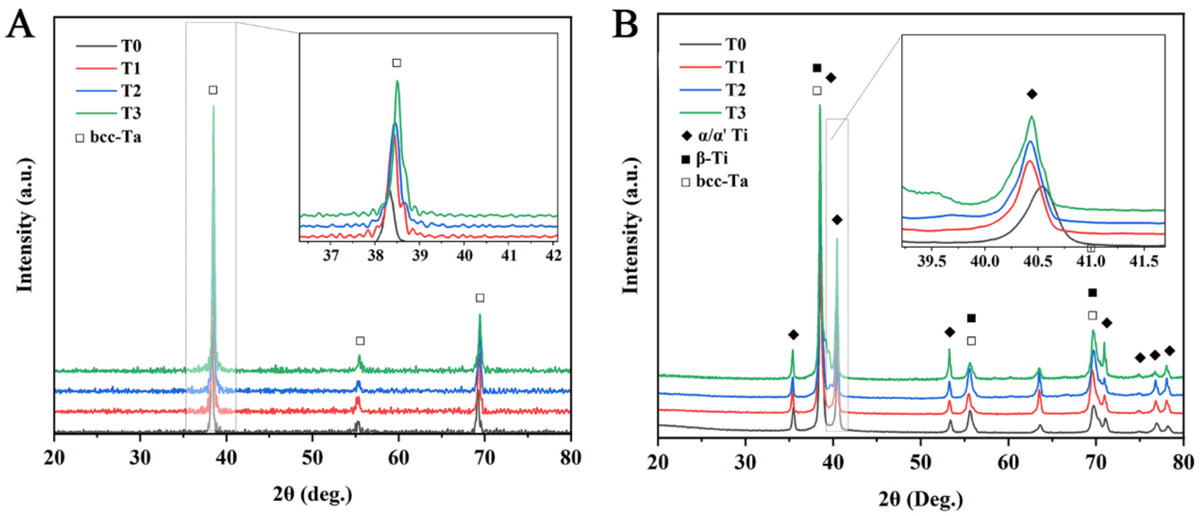

Figure 13. XRD patterns of bimetallic materials under different heat treatments: (A) the Ta side of the Ti-6Al-4V/Ta bimetal; and (B) The Ti-6Al-4V/Ta interface area. XRD: X-ray diffractometer.

(1) The residual stress measured in the Ta part of the bimetal (Point 1) was similar to or slightly higher than that of the as-printed pure Ta.

(2) A compressive residual stress of ~ (30-70) MPa was recorded near the interface of the as-printed bimetal (Point 2), differing greatly from the higher tensile stress (~ 100 MPa) observed in the pure Ta (Point 1 and Figure 12).

(3) A high residual tensile stress (~ 350-390 MPa) was detected around Point 3, that is, inside the as-printed Ti-6Al-4V.

Microstructure and properties of heat-treated Ti-6Al-4V/Ta bimetal

Microstructure and interface characterization of heat-treated Ti-6Al-4V/Ta bimetal

As demonstrated by the results in the above section, there is a high level of residual stress in the as-printed bimetal, which is also nonhomogeneous and likely to induce premature fracture. As for most other as-printed materials, this can be rectified by heat treatment. The bimetal samples were subjected to various heat treatment regimens. Figure 13A shows the XRD patterns of the Ta side of the Ti-6Al-4V/Ta bimetal in the as-printed state (T0) and after heat treatment at 550 °C (T1), 750 °C (T2), and 950 °C (T3). Diffraction peaks corresponding to bcc-Ta were detected in all samples. When the heat treatment temperature increased from 550 °C to 950 °C, the diffraction peak of bcc-Ta shifted significantly to the right, most likely due to a reduction in residual stress. In addition, with an increase in the heat treatment temperature, the diffraction peak width of the bcc-Ta phase increased slightly, indicating an enlarged grain size after heat treatment. Figure 13B shows the XRD patterns of the area around the Ti-6Al-4V/Ta interface. The $(0002)_{\alpha\text{-Ti}}$ diffraction peak shifted left as the heat treatment temperature increased, suggesting heat treatment may have caused Ta atoms to diffuse into the Ti matrix.

Nanohardness and tensile properties of heat-treated Ti-6Al-4V/Ta bimetal

The nanoindentation hardness of the interface area of the Ti-6Al-4V/Ta bimetals in the as-printed and heat-treated states was evaluated, and the results are shown in Figure 14. The nanohardness of the Ta decreased from ~ 3.4 GPa in the as-printed state to ~ 2.7 GPa after heat treatment. The nanohardness of the

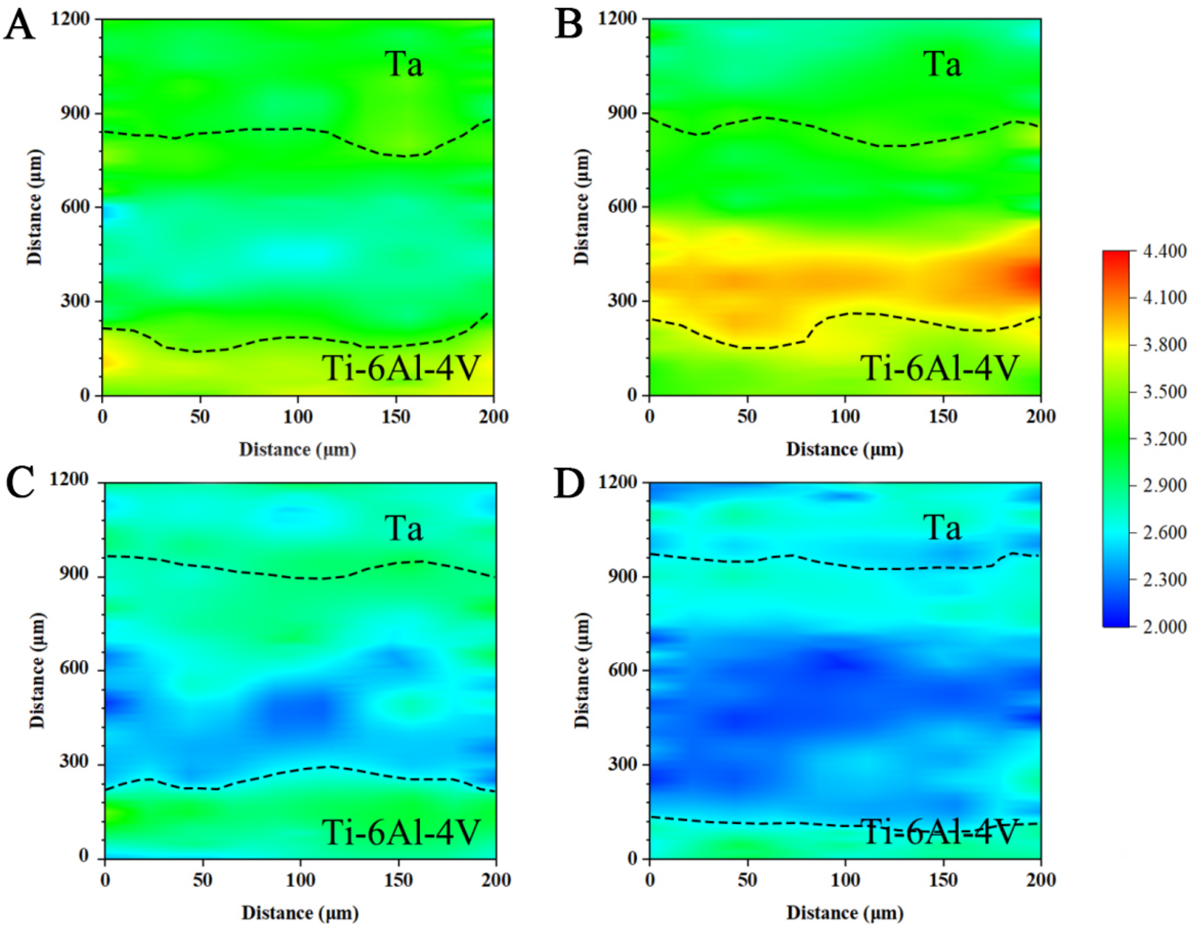

Figure 14. Nanohardness mapping results for the bimetal under different heat treatments: (A) As-printed; (B) 550 °C; (C) 750 °C; and (D) 950 °C.

Ti-6Al-4V matrix also decreased. The 550 °C heat treatment case differed from the others, exhibiting a high nanohardness of up to ~ 4.4 GPa. This is likely attributed to the residual stress detected in the local area.

Figure 15 shows the stress-strain curves of the as-printed and heat-treated bimetals. Heat treatment at 550 °C resulted in the highest tensile strength (~ 1,044 MPa) but the lowest elongation (2.82%). Higher heat treatment temperatures reduced the tensile strength and increased the elongation at break. At temperatures of 750 °C and 950 °C, the corresponding strengths are 908 MPa and 860 MPa, with elongations of 5.24% and 6.81%, respectively. As shown in Table 7[40], the performance of the heat-treated Ti-6Al-4V/Ta bimetal was close to that of the annealed Ti-6Al-4V.

Wear resistance of heat-treated Ti-6Al-4V/Ta bimetal

Room-temperature friction and wear tests were conducted on the as-printed and heat-treated bimetals, and the results were compared with those for as-printed Ti-6Al-4V. Figure 16A shows the wear track depth and width curves of the different samples. The average wear rate was calculated using the wear volume of the sample and the reciprocating stroke during the wear test, as shown in Equation 3[41].

$$K_v = \frac{V_{\mathrm{uear}}}{SF_N} \tag{3}$$

where K_v represents the wear rate (mm^3/Nm); V_{wear} is the wear volume (mm^3); S is the travel distance (m); and F_N is the applied normal load (N).

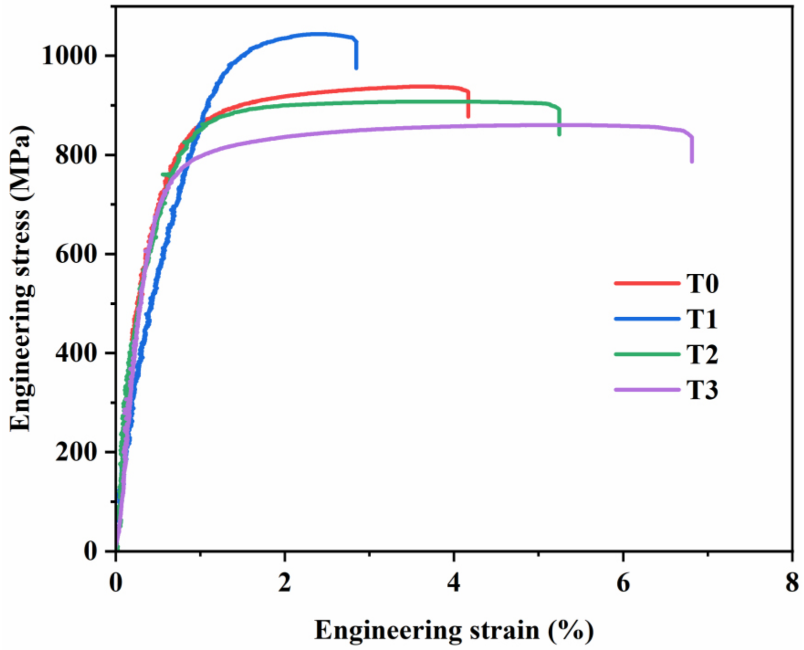

Figure 15. Room temperature tensile curves of the bimetal under different heat treatments.

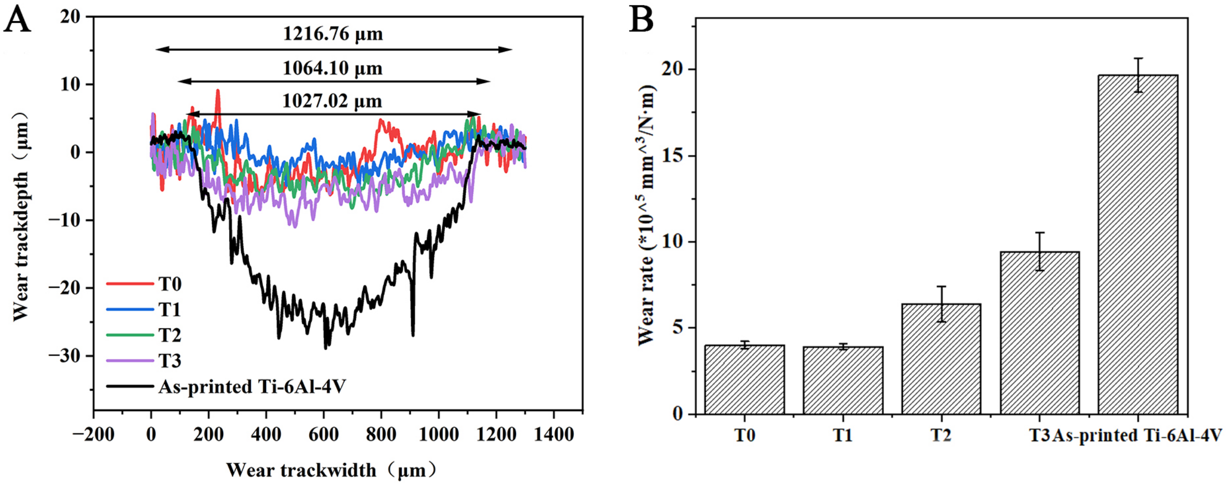

Figure 16. Wear properties of the bimetal under different heat treatments: (A) wear profile and (B) average wear rate. The error bars represent the standard deviation.

Table 7. Results of bimetallic room temperature tensile test[40]

	T0	T1	T2	T3	SLM Ti-6Al-4V[40]		
Status	As-printed	550°C	750°C	950°C	600°C	800°C	900°C
Tensile strength /MPa	938	1044	908	860	959	802	689.5
Elongation/%	4.17	2.82	5.24	6.81	8.3	6.8	6.5

Figure 16B compares the wear rates of the as-printed and heat-treated samples with each other and with that of the base Ti64 alloy. The wear rate of the sample heat-treated at 550 °C was virtually identical to that of the as-printed bimetal, measured at 4.02×10^{-5} mm^3/Nm and 3.94×10^{-5} mm^3/Nm, respectively. As the heat treatment temperature increased, the average wear rate rose to 6.39×10^{-5} mm^3/Nm and 9.43×10^{-5} mm^3/Nm

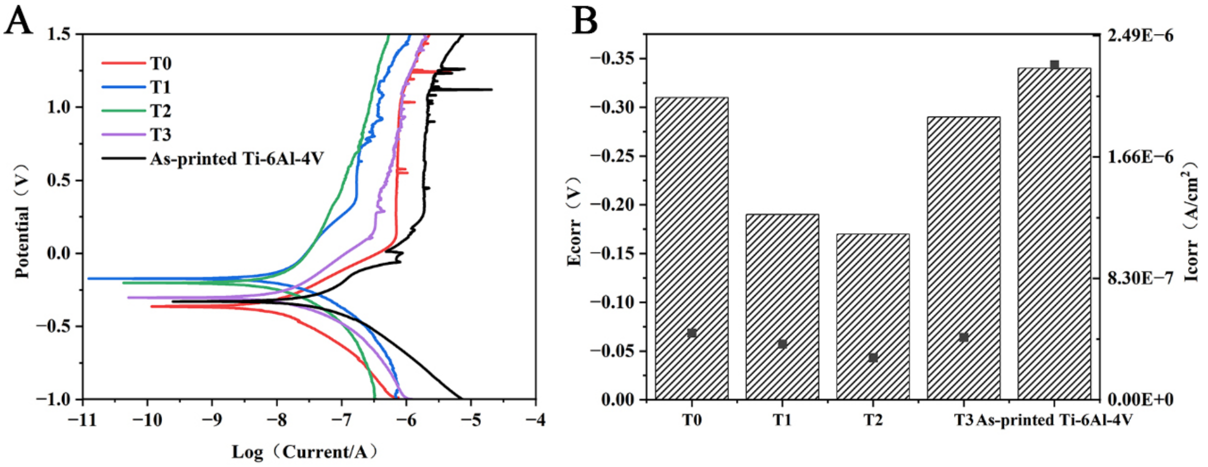

Figure 17. (A) Tafel curve of the potentiodynamic polarization curves of the bimetallic in the SBF solution and under different heat treatments; and (B) corrosion voltage and corrosion current. SBF: Simulated body fluid.

Table 8. Polarization results of the different samples

	T0	T1	T2	T3	As-printed Ti-6Al-4V
E_{corr}(V)	-0.31	-0.19	-0.17	-0.29	-0.34
I_{corr}(A/cm^2)	4.57 × 10^{-7}	3.81 × 10^{-7}	2.88 × 10^{-7}	4.27 × 10^{-7}	2.29 × 10^{-6}
S_{corr}(mm/y)	3.24 × 10^{-4}	2.71 × 10^{-4}	2.04 × 10^{-4}	3.03 × 10^{-4}	2.02 × 10^{-3}

for samples treated at 750 °C and 950 °C, respectively. Compared to the as-printed Ti-6Al-4V alloy, all bimetal samples exhibited significantly improved wear resistance.

Corrosion resistance of the heat-treated Ti-6Al-4V/Ta bimetal

Figure 17A and B shows the electrochemical corrosion behavior of the different bimetals, as well as that of the as-printed Ti-6Al-4V, measured using the controlled potential method in an SBF solution at 37 °C. The corrosion rate can be indirectly assessed using the self-corrosion current density, which follows Faraday's law, as shown in Equation 4[42,43]:

$$S_{\text{corr}} = \frac{I_{\text{corr}} \times A}{F \times n \times \rho} \tag{4}$$

where S_{corr} is the metal corrosion rate, I_{corr} is the corrosion current density, A is the relative atomic mass of the metal, F is the Faraday constant, n is the number of electrons lost from the metal, and ρ is the density of the metal.

The self-corrosion current density was determined by extrapolating the Tafel region of the polarization curve. When using Tafel fitting in Zview, key parameters such as the corrosion potential (E_{corr}), anodic and cathodic Tafel slopes (β_a/β_c), and initial corrosion current (I_{corr}) should be selected. The precise values were obtained through iterative convergence using the least squares method. Table 8 lists the self-corrosion current densities and voltages after fitting and converting the Tafel curves. Compared to the as-printed Ti-6Al-4V, the as-printed bimetal (T0) already exhibited superior corrosion resistance. Specifically, its E_{corr} increased from -0.34 V to -0.31 V, while the I_{corr} significantly decreased from 2.29 × 10^{-6} A/cm^2 to 4.57 × 10^{-7} A/cm^2. Correspondingly, the corrosion rate dropped markedly from 2.02 × 10^{-3} mm/y to 3.24 × 10^{-4} mm/y, indicating that Ta inherently possesses better electrochemical stability in corrosive environments.

In general, heat treatment improved the corrosion resistance of the bimetallic samples, resulting in a decrease in corrosion current. With increasing heat treatment temperatures, the corrosion resistance of Ta improved progressively in the T1 (550 °C) and T2 (750 °C) samples. Among them, T2 exhibited the best performance, with the highest E_{corr} (-0.17 V), the lowest I_{corr} (2.88×10^{-7} A/cm²), and the lowest corrosion rate (2.04×10^{-4} mm/y), reflecting optimal electrochemical stability. In contrast, at an even higher temperature (T3, 950 °C), the I_{corr} of the T3 sample slightly increased, with a corresponding corrosion rate of 3.03×10^{-4} mm/y. Although marginally inferior to T2, its performance still surpassed that of the untreated sample. A possible reason is that excessively high heat treatment temperature may cause inward diffusion of O atoms from the surface oxide layer, leaving corrosion channels in their wake and thereby slightly reducing the sample's resistance to corrosion.

In vitro biocompatibility of the heat-treated Ti-6Al-4V/Ta bimetal

The initial adhesion of MG-63 cells on the various printed bimetal samples over 2 h was assessed using SEM, as shown in Figure 18A-D. Most MG-63 cells, except for the printed Ti-6Al-4V/Ta, exhibited a flat spherical/prismatic shape with a diameter of approximately 30 μm. More notably, the MG-63 cells had many filamentous filopodia extensions on the surfaces of the bimetallic samples, whereas fewer filamentous filopodia extensions were observed on the Ti64 sample. The cell dispersion was similar for all samples, but cell-to-cell communication and adhesion were more pronounced on the bimetallic sample and bimetallic sample treated at 950 °C. It is well established that cell adhesion to material surfaces is regulated by both surface chemistry and topology[44].

The *in vitro* cytocompatibility of all samples was investigated by measuring the cellular activity after culturing the MG-63 cells for 24 h, 72 h, and 120 h. The results are shown in Figure 18E. In comparison with the Ti-6Al-4V sample, the bimetallic samples showed higher cell proliferation rates at 72 h and 120 h, indicating that they significantly promote cell proliferation and have excellent biocompatibility. However, the biocompatibility of the bimetal samples decreased after heat treatment, likely due to changes in the physical and chemical properties of the surface oxide layer, which may have reduced their ability to interact with cells. Nevertheless, these results suggest that bimetals exhibit superior biocompatibility compared to Ti-6Al-4V.

Discussion

The above experiments indicate that when printed using optimized parameters, the Ti-6Al-4V/Ta bimetal achieves a series of favorable properties, including high fracture strength, superior wear and corrosion resistance, and improved biocompatibility. Compared with pure Ti-6Al-4V, the Ta layer plays a crucial role in improving wear and corrosion resistance, as well as biocompatibility. On one hand, the improved wear resistance by the Ta layer can be explained by the formation of tantalum oxides during localized short-term heating caused by frictional interaction with the counter body. These oxides reduce friction and thereby contribute to improved wear resistance[45]. On the other hand, the superior corrosion resistance is also related to tantalum oxide, which is more chemically stable than titanium oxide. The tantalum oxide layer can prevent Cl^- ions in the SBF solution from penetrating the passive film and initiating pitting corrosion[46]. Moreover, the improved biocompatibility can be attributed to the intrinsic excellent biocompatibility of element Ta. The Ta layer also acts as a barrier, preventing the diffusion of cytotoxic Al and V ions into surrounding tissues or tissue fluids. These improved properties are closely related to the unique structural characteristics of the Ti-6Al-4V/Ta bimetal, which are strongly influenced by residual stress and interfacial bonding.

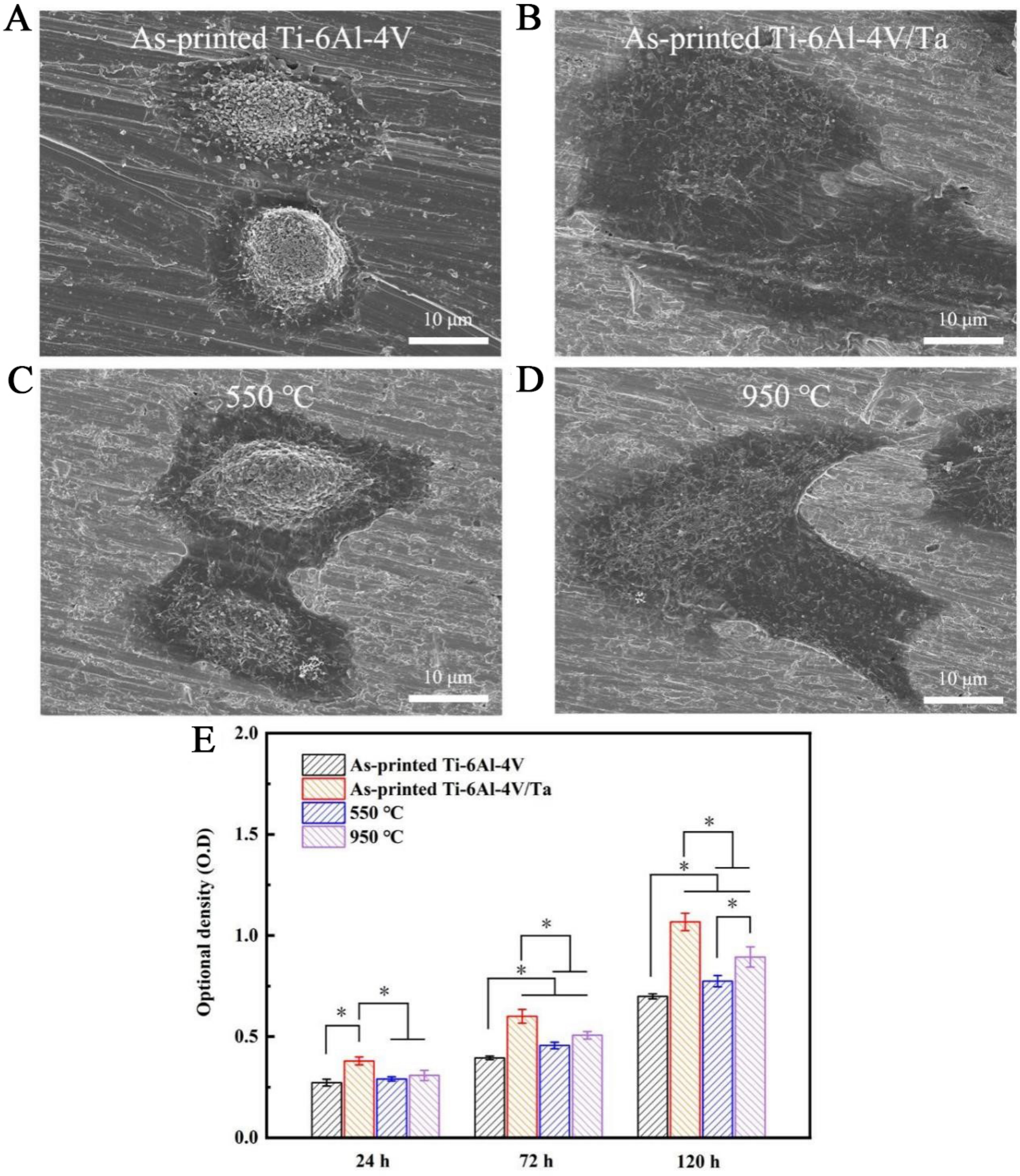

Figure 18. SEM images showing cell adhesion after 2 h of culture on bimetal and as-printed Ti-6Al-4V under different heat treatments: (A) as-printed Ti-6Al-4V; (B) As-printed Ti-6Al-4V/Ta; (C) Heat-treated at 550 °C; and (D) heat-treated at 950 °C; (E) Proliferation of MG-63 cells on the bimetals under different heat treatments after 24 h, 72 h, and 120 h of culture (*$P < 0.05$) (For each condition, five samples were studied). The error bars represent the standard deviation. SEM: Scanning electron microscope.

Residual stress

Generally speaking, residual stress due to thermal gradient is proportional to $(\Delta T \cdot \alpha \cdot E)$, where ΔT is the temperature gradient, α is the coefficient of thermal expansion, and E is the Young's modulus[47]. In the above section, a change from tensile to compressive residual stress was observed in the as-printed Ta alone and the interface area in the as-printed bimetal. Based thereon, the following analysis is made:

(1) The absolute value of the residual stress in the interface area region of the bimetal was reduced compared to the plain Ta. This is attributed to two reasons: the lowered temperature gradient and a lower Young's modulus. Regarding the former, the Ta part of the bimetal was printed on top of a freshly printed Ti-6Al-4V substrate. The newly deposited alloy is likely to have been at a higher temperature than the substrate of a normal printing condition (often approximately 200 °C). Regarding the latter, the inter-diffusion of Ta atoms and Ti/Al/V atoms during printing is likely to have reduced the Young's modulus of the Ta part of the bimetal because of the lower Young's modulus of Ti-6Al-4V.

(2) The change from tensile to compressive residual stress is most likely caused by changes in the lattice parameters, which affect plane distance and, eventually, the residual stress status. This is also possible to have been exacerbated by the fact that Ta has an atomic radius of ~ 217 ppm and Ti has an atomic radius of ~ 187 ppm[48]. The diffusion of Ti atoms into the Ta lattices and the replacement of Ta atoms decreased the lattice parameters, thereby changing the residual stress from tensile to compressive.

Interface bonding in bimetal

As mentioned before (e.g., Figure 7), a COMSOL simulation was conducted to determine the optimal printing parameters for the Ti-6Al-4V/Ta bimetal. The resulting parameters were predicted to achieve a molten pool temperature of up to ~ 3,500 K, which, from an energy perspective, is high enough to remelt the Ta powder and create the Ti-6Al-4V/Ta bimetal. Theoretical analysis of the depth of the molten pool can also assist in understanding the bimetal formation. This was done using the model developed by Tang *et al.*[49]:

$$D = \frac{W}{2} = \sqrt{\frac{2AP}{\mathrm{en}\,\rho C\,(T_m - T_0)\,v}} \tag{5}$$

where W and D are the melt pool width and depth, respectively; A is the laser absorptivity (assumed to be 0.374 for the Ta powder bed); ρ is the material density; C is the material's thermal capacity; v is scanning speed; T_m is the material's melting temperature; and T_0 is the substrate temperature.

Under the optimized parameters (*i.e.*, laser power of 200 W and scanning speed of 0.33 m/s), the corresponding D and W values were calculated as: D = 87.4 μm and W = 174.8 μm.

The following observations were made from the molten pool simulation results.

(1) Since the layer thickness used in the study is only 30 μm, the ~ 80 μm molten pool depth ensures that the very few first layers of Ta that have been deposited on top of the Ti-6Al-4V matrix have a good chance to inter-diffuse and bond with the high-temperature Ti phase (the β-Ti phase).

(2) In the printing experiments, the width of the interface area was recorded to be approximately 800 μm (see the microstructural analysis in Figure 8). This was much higher than the simulated molten pool depth, implying that a full layer of Ta was created only after approximately 26-layer powder depositions. This is understandable, considering that the vacancy of the powder bed can normally be ~ 30 vol.%, leaving a large amount of open space to be filled by the next layer of material. Furthermore, Ta has a much higher density than Ti, which also contributes to the downward movement of Ta atoms and the enlargement of the bonding area.

(3) Ti and Ta have infinite solubility in one another [Figure 19], which is often beneficial for forming good metallurgical bonds without brittle intermetallics.

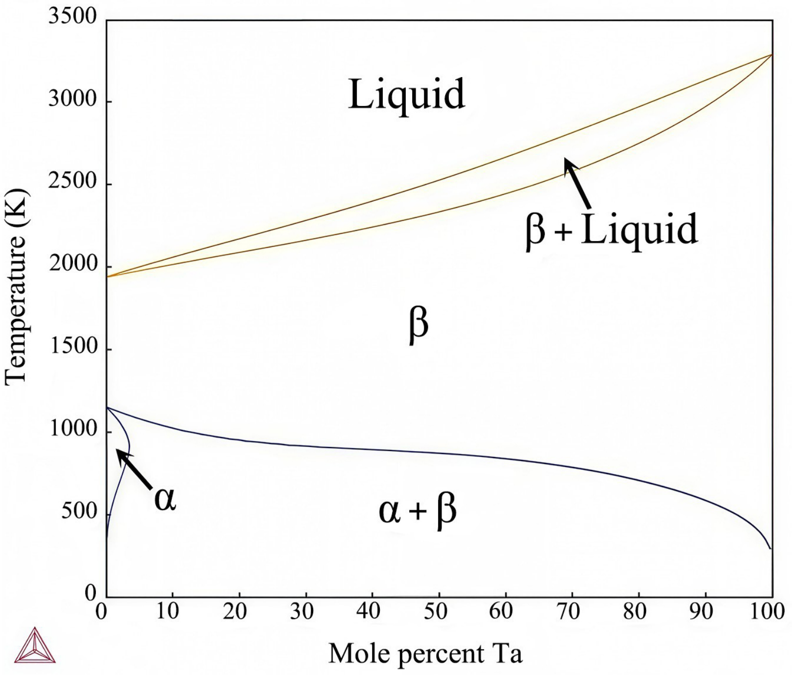

Figure 19. Binary phase diagram of Ti-Ta.

(4) Compressive residual stress defected in the interface area of the as-printed bimetal may have also contributed to a good bonding [Figure 13].

CONCLUSIONS

In this study, a Ti-6Al-4V/Ta bimetal was additively manufactured using a PBF-LB printer. Optimal printing parameters and residual stress were studied for the bimetal, based on which the mechanical properties and microstructure of the as-printed and heat-treated samples were further investigated. The bimetal's wear resistance, corrosion resistance, and biocompatibility were also evaluated. The key findings are summarized below.

Optimized printing parameters for the Ti-6Al-4V/Ta bimetal were determined based on the relative density and porosity of the bonding interface. A laser power of 200 W and a scanning speed of 330 mm/s yielded a pore-free bonding interface with a relative density of ~ 99.5%.

(1) Owing to its high density, the as-printed bimetal exhibited a tensile strength of ~ 934 MPa and an elongation at fracture of 4.17%. After heat treatment at 550 °C for 2 h, the tensile strength increased to 1,044 MPa, but the elongation at break decreased to 2.82%. When the heat treatment temperature exceeded 750 °C, the tensile strength showed a slight decline, whereas the elongation at break increased.

(2) A high tensile residual stress (up to 390 MPa) was detected in the Ti-6Al-4V part of the as-printed bimetal. The residual stress inside the Ta part and near the interface area of the as-printed bimetal was reduced to ~ (3070) MPa under compressive stress, compared to the ~ (140-180) MPa tensile stress recorded in the as-printed Ta alone. The compressive residual stress may have contributed to the success of the bonding between the Ta layer and the Ti-6Al-4V matrix.

(3) Regarding corrosion resistance, the as-printed bimetal exhibited a corrosion current density of 4.57×10^{-7}

A/cm^2 in an SBF, representing a significant improvement over the as-printed Ti-6Al-4V (2.29×10^{-6} A/cm^2). Heat treatment further enhanced the corrosion resistance, achieving a minimum corrosion rate of 2.04 × 10-4 mm/y.

(4) The as-printed and heat-treated bimetals achieved wear rates of ~ 4×10^{-5} mm^3/Nm, demonstrating a much-improved wear resistance compared to the as-printed Ti-6Al-4V (wear rate = 1.97×10^{-4} mm^3/Nm).

DECLARATIONS

Acknowledgement

The authors would like to acknowledge the technical support from SUSTech CRF.

Authors' contributions

Data acquisition and analysis: Wang, H.; Ma, K.; Tang, J.; Zhao, J.; Chen, H.; Hao, J.; He, L.
Conception and design of this study: Wang, H.; Zhou, Y.; Luo, X.; Yan, M.
Writing: Wang, H.; Ma, K.; Zhou, Y.; Luo, X.; Yan, M.
Supervision: Zhou, Y.; Luo, X.; Yan, M.

Availability of data and materials

Experimental data of this study will be available from the corresponding authors upon reasonable request.

AI and AI-assisted tools statement

Not applicable.

Financial support and sponsorship

This work was supported by the Key Research and Development Program of Jiangsu Province (No. K22251901), National Natural Science Foundation of China (No. 52271032), and Shenzhen Science and Technology Innovation Commission (No. JCYJ20220818100612027).

Conflicts of interest

The authors declared that there are no conflicts of interest.

Ethical approval and consent to participate

Not applicable.

Consent for publication

Not applicable.

Copyright

Supplementary Materials

Supplementary Materials

REFERENCES

1. Tang, J.; Wu, Z.; Yao, X.; et al. From bio-inertness to osseointegration and antibacterial activity: A one-step micro-arc oxidation approach for multifunctional Ti implants fabricated by additive manufacturing. *Mater. Des.* **2022**, *221*, 110962. DOI
2. Salehi, M.; Malekan, M.; Montazeri, A. Comprehensive study of sub-micron porous titanium-zirconium scaffolds fabricated by liquid metal dealloying. *J. Alloys. Compd.* **2025**, *1010*, 177137. DOI
3. Long, M.; Rack, H. J. Titanium alloys in total joint replacement - a materials science perspective. *Biomaterials* **1998**, *19*, 1621-39. DOI PubMed
4. Ungersboeck, A.; Geret, V.; Pohler, O.; Schuetz, M.; Wuest, W. Tissue reaction to bone plates made of pure titanium: a prospective, quantitative clinical study. *J. Mater. Sci:. Mater. Med.* **1995**, *6*, 223-9. DOI
5. Wang, K. The use of titanium for medical applications in the USA. *Mater. Sci. Eng:. A.* **1996**, *213*, 134-7. DOI

6. Rieu, J.; Pichat, A.; Rabbe, L.; Rambert, A.; Chabrol, C.; Robelet, M. Structural modifications induced by ion implantation in metals and polymers used for orthopaedic prostheses. *Mater. Sci. Technol.* **1992**, *8*, 589-93. DOI
7. Wang, C.; Zheng, C.; Rang, J. Joint replacement materials and friction wear. *J. Biomed. Eng.* **1997**, *14*, 64-67. (in Chinese).
8. Levine, B. R.; Sporer, S.; Poggie, R. A.; Della, Valle. C. J.; Jacobs, J. J. Experimental and clinical performance of porous tantalum in orthopedic surgery. *Biomaterials* **2006**, *27*, 4671-81. DOI PubMed
9. Bermúdez, M.; Carrión, F. J.; Martínez-nicolás, G.; López, R. Erosion-corrosion of stainless steels, titanium, tantalum and zirconium. *Wear* **2005**, *258*, 693-700. DOI
10. Charoenpong, H.; Ritprajak, P. Effect of metal ions released from orthodontic mini-implants on osteoclastogenesis. *Dent. Med. Probl.* **2021**, *58*, 327-33. DOI PubMed
11. Asri, R. I. M.; Harun, W. S. W.; Samykano, M.; et al. Corrosion and surface modification on biocompatible metals: A review. *Mater. Sci. Eng. C. Mater. Biol. Appl.* **2017**, *77*, 1261-74. DOI
12. Matsuno, H.; Yokoyama, A.; Watari, F.; Uo, M.; Kawasaki, T. Biocompatibility and osteogenesis of refractory metal implants, titanium, hafnium, niobium, tantalum and rhenium. *Biomaterials* **2001**, *22*, 1253-62. DOI PubMed
13. Zhou, L.; Yuan, T.; Li, R.; Tang, J.; Wang, G.; Guo, K. Selective laser melting of pure tantalum: Densification, microstructure and mechanical behaviors. *Mater. Sci. Eng:. A.* **2017**, *707*, 443-51. DOI
14. Yang, Y.; Zhang, J.; Wei, W. Microstructure and mechanical properties of TiC/Ti6Al4V nanocomposites fabricated by gas-liquid reaction laser powder bed fusion. *Mater. Sci. Eng:. A.* **2023**, *869*, 144829. DOI
15. Lei, P.; Qian, H.; Zhang, T.; et al. Porous tantalum structure integrated on Ti6Al4V base by laser powder bed fusion for enhanced bony-ingrowth implants: *in vitro* and *in vivo* validation. *Bioact. Mater.* **2022**, *7*, 3-13. DOI PubMed PMC
16. Lian, F.; Chen, L.; Wu, C.; Zhao, Z.; Tang, J.; Zhu, J. Selective laser melting additive manufactured tantalum: effect of microstructure and impurities on the strengthening-toughing mechanism. *Materials. (Basel).* **2023**, *16*, 3161. DOI PubMed PMC
17. Valentino, G. M.; Banerjee, A.; Lark, A.; Barr, C. M.; Myers, S. H.; Mccue, I. D. Influence of laser processing parameters on the density-ductility tradeoff in additively manufactured pure tantalum. *Addit. Manuf. Lett.* **2023**, *4*, 100117. DOI
18. Song, C.; Deng, Z.; Zou, Z.; Liu, L.; Xu, K.; Yang, Y. Pure tantalum manufactured by laser powder bed fusion: influence of scanning speed on the evolution of microstructure and mechanical properties. *Int. J. Refract. Met. Hard. Mater.* **2022**, *107*, 105882. DOI
19. Livescu, V.; Knapp, C. M.; Gray, G. T.; Martinez, R. M.; Morrow, B. M.; Ndefru, B. G. Additively manufactured tantalum microstructures. *Materialia* **2018**, *1*, 15-24. DOI
20. Gao, H.; Yang, J.; Jin, X.; et al. Porous tantalum scaffolds: Fabrication, structure, properties, and orthopedic applications. *Mater. Des.* **2021**, *210*, 110095. DOI
21. Wauthle, R.; van, der. Stok. J.; Amin, Yavari. S.; et al. Additively manufactured porous tantalum implants. *Acta. Biomater.* **2015**, *14*, 217-25. DOI
22. Walker, J.; Middendorf, J. R.; Lesko, C. C.; Gockel, J. Multi-material laser powder bed fusion additive manufacturing in 3-dimensions. *Manuf. Lett.* **2022**, *31*, 74-7. DOI
23. Lesko, C.; Walker, J.; Middendorf, J.; Gockel, J. Functionally graded titanium-tantalum in the horizontal direction using laser powder bed fusion additive manufacturing. *JOM* **2021**, *73*, 2878-84. DOI
24. Traxel, K. D.; Bandyopadhyay, A. Modeling and experimental validation of additively manufactured tantalum-titanium bimetallic interfaces. *Mater. Des.* **2021**, *207*, 109793. DOI
25. Huang, S.; Sing, S. L.; de, Looze. G.; Wilson, R.; Yeong, W. Y. Laser powder bed fusion of titanium-tantalum alloys: compositions and designs for biomedical applications. *J. Mech. Behav. Biomed. Mater.* **2020**, *108*, 103775. DOI PubMed
26. Yan, J. J.; Zheng, D. L.; Li, H. X.; et al. Selective laser melting of H13: microstructure and residual stress. *J. Mater. Sci.* **2017**, *52*, 12476-85. DOI
27. Shabalin, I. L. Tantalum. In *Ultra-high temperature materials I: Carbon (graphene/graphite) and refractory metals,* Springer,2014; pp. 387-450. DOI
28. Balla, V. K.; Banerjee, S.; Bose, S.; Bandyopadhyay, A. Direct laser processing of a tantalum coating on titanium for bone replacement structures. *Acta. Biomater.* **2010**, *6*, 2329-34. DOI PubMed PMC
29. Ren, Y.; Lin, X.; Fu, X.; Tan, H.; Chen, J.; Huang, W. Microstructure and deformation behavior of Ti-6Al-4V alloy by high-power laser solid forming. *Acta. Materialia.* **2017**, *132*, 82-95. DOI
30. Tang, Y.; Liu, Y.; Peng, Y.; Xiong, W.; Long, J.; Tan, D. Dynamic restoration and texture evolution of pure tantalum during warm deformation. *Int. J. Refract. Met. Hard. Mater.* **2023**, *115*, 106279. DOI
31. Yan, M.; Yu, P. An overview of densification, Microstructure and mechanical property of additively manufactured Ti-6Al-4V - comparison among selective laser melting, electron beam melting, laser metal deposition and selective laser sintering, and with conventional powder. In: Lakshmanan A, editor. *Sintering. Techniques. of. Materials,.* , 2015. DOI

32. Pant, P.; Proper, S.; Luzin, V.; et al. Mapping of residual stresses in as-built Inconel 718 fabricated by laser powder bed fusion: A neutron diffraction study of build orientation influence on residual stresses. *Addit. Manuf.* **2020**, *36*, 101501. DOI
33. Nycz, A.; Lee, Y.; Noakes, M.; et al. Effective residual stress prediction validated with neutron diffraction method for metal large-scale additive manufacturing. *Mater. Des.* **2021**, *205*, 109751. DOI
34. Heeling, T.; Cloots, M.; Wegener, K. Melt pool simulation for the evaluation of process parameters in selective laser melting. *Addit. Manuf.* **2017**, *14*, 116-25. DOI
35. Menon, N.; Basak, A. Prediction of melt pool geometry by fusing experimental and simulation data. *Int. J. Mech. Sci.* **2024**, *263*, 108786. DOI
36. Chen, C.; Xia, X.; Yang, S.; et al. Effect of the thickness of Ti intermediate layer on the microstructure and mechanical properties of the W/Ta multilayer composites. *J. Alloys. Compd.* **2021**, *867*, 158910. DOI
37. Standardization Administration of China. GB/T 8546-2017: Titanium clad stainless steel plate, Beijing: Standards Press of China; 2017.
38. Zhou, Y. L.; Niinomi, M.; Akahori, T. Effects of Ta content on young’s modulus and tensile properties of binary Ti-Ta alloys for biomedical applications. *Mater. Sci. Eng:. A.* **2004**, *371*, 283-90. DOI
39. Sing, S. L.; Yeong, W. Y.; Wiria, F. E. Selective laser melting of titanium alloy with 50 wt% tantalum: Microstructure and mechanical properties. *J. Alloys. Compd.* **2016**, *660*, 461-70. DOI
40. Song, M. L. Effect of laser selective melting process and subsequent heat treatment on the microstructure and properties of Ti-6Al-4V alloy, Shandong University, Master Degree Thesis, Shandong University, Jinan, Shandong, 2021. DOI
41. Schmidt, A. A.; Schmidt, T.; Grabherr, O.; Bartel, D. Transient wear simulation based on three-dimensional finite element analysis for a dry running tilted shaft-bushing bearing. *Wear* **2018**, *408-9*, 171-9. DOI
42. Lin, K.; Qiao, J.; Gu, D.; et al. Active screen plasma nitriding of laser powder bed fusion processed 316L stainless steel for the application of fuel cell bipolar plates. *Virtual. Phys. Prototyp.* **2023**, *18*, e2225490. DOI
43. Shuai, C.; He, C.; Feng, P.; et al. Biodegradation mechanisms of selective laser-melted Mg- *x* Al-Zn alloy: grain size and intermetallic phase. *Virtual. Phys. Prototyp.* **2018**, *13*, 59-69. DOI
44. Gui, N.; Xu, W.; Myers, D. E.; Shukla, R.; Tang, H. P.; Qian, M. The effect of ordered and partially ordered surface topography on bone cell responses: a review. *Biomater. Sci.* **2018**, *6*, 250-64. DOI
45. Burkov, A. A.; Nikolenko, S. V.; Krutikova, V. O.; Shelmenok, N. A. Electrospark Deposition of Ti-Ta coatings on Ti6Al4V titanium alloy: oxidation resistance and wear properties. *Phys. Mesomech.* **2024**, *27*, 618-26. DOI
46. Zhao, D.; Han, C.; Li, Y.; et al. Improvement on mechanical properties and corrosion resistance of titanium-tantalum alloys *in-situ* fabricated via selective laser melting. *J. Alloys. Compd.* **2019**, *804*, 288-98. DOI
47. Becker, T.; Cannon, R.; Ritchie, R. An approximate method for residual stress calculation in functionally graded materials. *Mech. Mater.* **2000**, *32*, 85-97. DOI
48. National Center for Biotechnology Information, 2024. Atomic Radius in the Periodic Table of Elements. Available from: https://pubchem.ncbi.nlm.nih.gov/periodic-table/atomic-radius (accessed 2025-6-5).
49. Tang, M.; Pistorius, P. C.; Beuth, J. L. Prediction of lack-of-fusion porosity for powder bed fusion. *Addit. Manuf.* **2017**, *14*, 39-48. DOI